

Enabling Iron-Based Highly Effective Electrochemical Water-Splitting and Selective Oxygenation of Organic Substrates through In Situ Surface Modification of Intermetallic Iron Stannide Precatalyst

Biswarup Chakraborty, Rodrigo Beltrán-Suito, J. Niklas Hausmann, Somenath Garai, Matthias Driess,* and Prashanth W. Menezes*

A strategy to overcome the unsatisfying catalytic performance and the durability of monometallic iron-based materials for the electrochemical oxygen evolution reaction (OER) is provided by heterobimetallic iron–metal systems. Monometallic Fe catalysts show limited performance mostly due to poor conductivity and stability. Here, by taking advantage of the structurally ordered and highly conducting FeSn₂ nanostructure, for the first time, an intermetallic iron material is employed as an efficient anode for the alkaline OER, overall water-splitting, and also for selective oxygenation of organic substrates. The electrophoretically deposited FeSn₂ on nickel foam (NF) and fluorine-doped tin oxide (FTO) electrodes displays remarkable OER activity and durability with substantially low overpotentials of 197 and 273 mV at 10 mA cm⁻², respectively, which outperform most of the benchmarking NiFe-based catalysts. The resulting superior activity is attributed to the in situ generation of α -FeO(OH)@FeSn₂ where α -FeO(OH) acts as the active site while FeSn₂ remains the conductive core. When the FeSn₂ anode is coupled with a Pt cathode for overall alkaline water-splitting, a reduced cell potential (1.53 V) is attained outperforming that of noble metal-based catalysts. FeSn₂ is further applied as an anode to produce value-added products through selective oxygenation reactions of organic substrates.

1. Introduction


Electrochemical water-splitting through the hydrogen evolution reaction (HER) and oxygen evolution reaction (OER) has been regarded as one of the most promising ways to generate hydrogen (H₂), a renewable fuel.^[1] However, the efficiency of water splitting is largely limited by the thermodynamically up-hill OER that requires multiple proton-coupled electron transfer steps with complex reaction kinetics.^[2] Consequently, large overpotentials are required to achieve the OER process making it the bottleneck of water splitting.^[3] In order to reduce the energy barrier of OER, efficient and durable electrocatalysts (anodes) that can display low overpotentials at higher current densities with fast reaction kinetics are desired.^[4] Although the electrochemical water splitting to produce oxygen (O₂) and H₂ with noble metal-based catalysts (RuO₂, IrO₂ for the OER and Pt for HER) currently remains successful, the design of cost-

effective, active and sustainable materials utilizing natural resources of nonprecious metals begins to be a central thrust in the advancement of OER and HER electrocatalysts.^[5] Recent success with Earth-abundant metal-based electro(pre)catalysts for water splitting mostly rely on transition metal-oxides,^[6] phosphates,^[7] chalcogenides,^[8] pnictides,^[9] borides,^[10] phosphites,^[11] and borophosphates.^[12]

Within the transition-metals, iron is the naturally most abundant in Earth's-crust.^[13] Besides its abundance, accessible multiple redox states and rich coordination chemistry has made iron a biologically significant metal ion and it is present as co-factor in many metalloenzymes.^[14] Taking this into account, several iron-based materials have been designed as photo^[15] and electrocatalysts for OER, especially, for alkaline water splitting,^[16] HER^[17] and nitrogen reduction.^[18] However, poor electrical conductivity,^[16a] the tendency of iron to leach into the solution as a thermodynamically stable soluble (FeO₄)²⁻ species (as predicted by Pourbaix diagram),^[19] and a nonoptimal oxophilicity of iron in comparison to other transition metals limits its efficiency

Dr. B. Chakraborty, R. Beltrán-Suito, J. N. Hausmann, Prof. M. Driess, Dr. P. W. Menezes
Department of Chemistry: Metalorganics and Inorganic Materials
Technische Universität Berlin
Straße des 17 Juni 135, Sekr. C2, Berlin 10623, Germany
E-mail: matthias.driess@tu-berlin.de; prashanth.menezes@mailbox.tu-berlin.de

Dr. S. Garai
Department of Chemistry
National Institute of Technology
Tiruchirappalli, Tamil Nadu 620015, India

 The ORCID identification number(s) for the author(s) of this article can be found under <https://doi.org/10.1002/aenm.202001377>.

© 2020 The Authors. Published by WILEY-VCH Verlag GmbH & Co. KGaA, Weinheim. This is an open access article under the terms of the Creative Commons Attribution-NonCommercial-NoDerivs License, which permits use and distribution in any medium, provided the original work is properly cited, the use is non-commercial and no modifications or adaptations are made.

DOI: 10.1002/aenm.202001377

in alkaline OER catalysis.^[20] Such shortcomings can be overcome by the incorporation of iron into nickel^[21] or cobalt oxyhydroxides^[22] and currently, the mixed nickel–iron oxyhydroxides ($\text{Ni}_x\text{Fe}_{1-x}\text{OOH}$) are considered to be the most promising noble metal-free OER catalysts.^[23] Although the nature of the active site and the role of iron in the promotion of catalytic efficiency is still debatable,^[24] in-depth spectro-electrochemical, in situ and operando spectroscopic,^[25] as well as theoretical studies, predict a high-valent iron as the active species.^[26] Hence, unconventional catalysts based on iron that are strikingly active, highly conductive, and can sustain in the operating conditions by disfavoring iron dissolution are urgently needed to fulfil the void required for the next generation OER.^[27]

Similar to OER, electrooxidation of organic substrates to valuable chemicals has been regarded as a potential alternative to avoid hazardous chemical-oxidants and harsh reaction conditions. In this context, electrosynthesis of 2,5-furandicarboxylic acid (FDCA)^[28] is a value-added precursor for polymers such as polyethylene terephthalate and poly(ethylene 2,5-furandicarboxylate) and a convenient replacement of terephthalic acid. The electrooxidation of FDCA via selective oxidation of 5-hydroxymethylfurfural (HMF)^[29] is limited to noble metal-based electrodes.^[30] Although recent efforts to replace the noble-metal catalysts with transition metal-based materials have been made, the selectivity and efficiency of electrosynthesis of these biomass-derived organic products remain a great challenge.^[31] On the other hand, electrooxidation of ethanol to acetic acid, a high boiling solvent commonly used for organic synthesis, could also be efficiently performed only with noble-metal electrodes.^[32] Therefore, it is of significant interest to develop low-cost, non-noble metal-based, and high-performance catalysts that can unify both the kinetically sluggish OER and oxygenation reactions at the anode as well as continuous production of H_2 at the cathode by making the complete system energetically efficient.

Over the years, structurally ordered intermetallic compounds have gained enormous attention because of their unique crystallographic, chemical, physical and electronic properties, such as magnetism and superconductivity.^[33] As the arrangements of atoms in an intermetallic compound can be tailored to achieve superior electronic and adsorption properties, the interest has even grown in the last couple of years to explore intermetallics as active catalysts for application in electrocatalytic reactions.^[34] Within intermetallic compounds, metal stannides (MnSn_2 , FeSn_2 , and CoSn_2) have drawn special attention, as they possess a distinct connection pattern between the transition metal and tin atoms through covalent interactions leading to high electrical conductivity (metal-like character). In this regard, they have already been used successfully as anode materials for Li-ion batteries.^[35] Notably, intermetallics based on noble and non-noble metals have recently been utilized successfully for the reaction of OER, HER, and oxygen reduction reaction (ORR).^[36] Along this line, lately, a CoSn_2 nanostructure acting as a bifunctional electro(pre)catalyst for OER, HER and overall water-splitting in alkaline media has been reported resulting in substantially low overpotentials and high long-term stabilities.^[37] Furthermore, an improved electrocatalytic OER performance in both alkaline and neutral electrolyte has also been achieved after selenization of $\text{Cu}_3\text{Sn}@\text{Cu}$.^[38]

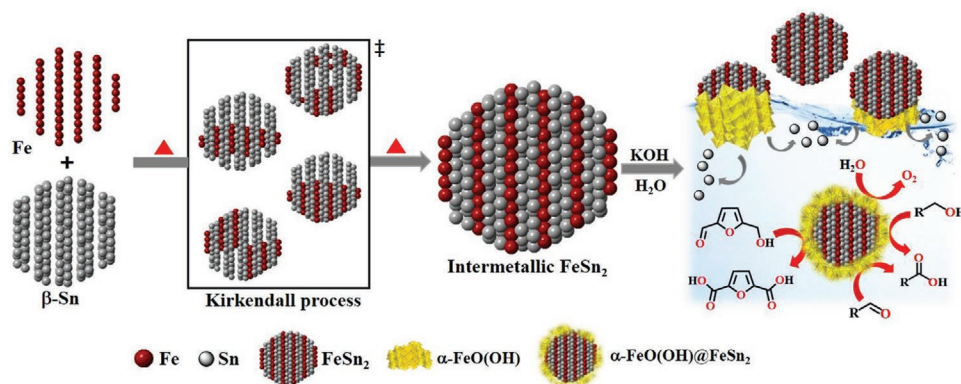
Motivated by these promising results, we aimed to investigate iron stannides as a promising class of anode materials for the kinetically demanding reactions of both OER and selective oxygenation.

Here, we report the synthesis of structurally ordered intermetallic iron stannide (FeSn_2) nanocrystals and apply them as highly active OER electro(pre) catalysts. The electrodeposited FeSn_2 on both fluorine-doped tin oxide (FTO) and nickel foam (NF) delivers superior OER performance in alkaline solutions. A detailed postcatalytic study infers that under electrochemical conditions, FeSn_2 endures surface restructuring and forms in situ $\alpha\text{-FeO}(\text{OH})@\text{FeSn}_2$ as the active catalyst. The superior performance of $\alpha\text{-FeO}(\text{OH})@\text{FeSn}_2$ over the similarly prepared Fe, reference $\text{Fe}(\text{OH})_3$, $\alpha\text{-FeO}(\text{OH})$, benchmark $\text{Ni}_x\text{Fe}_{1-x}\text{O}_4$ as well as state-of-the-art RuO_2 and IrO_2 catalysts highlights the essential role of the $\alpha\text{-FeO}(\text{OH})$ surface as the active species and FeSn_2 as the conductive site to facilitate enhanced O_2 production. Moreover, a two-electrode cell constructed using Pt as the cathode and FeSn_2 as the anode ($\text{Pt}(-)/\text{FeSn}_2(\text{NF})$) also displayed a low cell potential for alkaline water electrolysis. Encouraged by this, we further utilize the FeSn_2 anode for the challenging electrooxidation reactions of i) ethanol to acetic acid, ii) acetaldehyde to acetic acid, and iii) 5-HMF to 2,5-FDCA, yielding high efficiencies.

2. Results and Discussion

Structurally ordered intermetallic FeSn_2 nanocrystals were synthesized by a one-pot reduction of iron and tin precursor using sodium borohydride (NaBH_4) in ethylene glycol (EG) at 170 °C (see the Experimental Section in the Supporting Information for details). At elevated temperature, the slow growth of intermetallic nanocrystals transpires by the interspersing of Fe into the interlayers of metallic Sn through a Kirkendall process (Scheme 1).^[39] Interestingly, this diffusion-controlled growth mechanism was implied to be the operative mechanism to isolate highly crystalline intermetallic stannide nanostructures from tetragonal $\beta\text{-Sn}$, where the shape of the nanostructure was controlled by the diffusion rate of the species.^[40] The solid-state structure of the as-prepared FeSn_2 was further evaluated by powder X-ray diffraction (PXRD) where the sharp reflections matched (Figure 1a) clearly with FeSn_2 (JCPDS 25-415) (Figure S1, Supporting Information). FeSn_2 crystallizes in the CuAl_2 structure type and belongs to the tetragonal, space group $I4/mcm$ (space group No. 140) with the lattice parameters: $a = 6.539(2)$ Å and $c = 5.325(2)$ Å. The crystal structure consists of Fe atoms forming chains parallel to the [001].^[41] Each Fe atom is at the center of a square antiprism formed by adjacent Sn atoms while each Sn atom has four nearest Fe neighbors, which are part of two neighboring chains (Figure S2, Supporting Information).^[42] Such building units are further connected by Fe–Sn–Fe bonds to produce a 3D network (Scheme 1 and Figure 1a, inset). The structure has also been often described based on the homoatomic Sn–Sn interactions as a network of tetrahedral stars or layered nets as well as interpenetrating graphite-like nets.^[52]

Transmission electron microscopic (TEM) images depicted the nanoscale features of the FeSn_2 particles (Figure S3,



Scheme 1. Schematic representation of the formation of structurally ordered intermetallic FeSn_2 and close packing of the individual atomic layers of Fe and Sn (tetragonal, $I4/mcm$). The ordered structure of FeSn_2 is built up via the intercalation of metallic Fe layers (red spheres) and $\beta\text{-Sn}$ layers (grey spheres) at elevated temperature via the Kirkendall process.^[43] Under alkaline electrochemical reaction conditions, a substantial restructuring occurs at the surface due to the slow depletion of Sn from the FeSn_2 nanostructure and subsequent in situ formation of highly active crystalline $\alpha\text{-Fe}^{\text{II}}\text{O}(\text{OH})@$ FeSn_2 to catalyze both OER and multiple organic oxidations.

Supporting Information), while high-resolution TEM analyses verified the crystallinity of the nanoparticles with an interplanar d-spacing around 0.23 nm corresponding to the (112) plane of FeSn_2 (Figure 1b,c). High crystallinity and phase-purity of the as-prepared FeSn_2 was also evidenced from the well-defined diffraction rings resolved in the selected area electron diffraction (SAED) pattern (Figure 1c). Scanning electron microscopic (SEM) images of the FeSn_2 (Figure 1d; Figure S4, Supporting Information) revealed aggregation of the monodispersed

nanoparticles. Homogeneous distribution of Fe and Sn in the particle was confirmed by energy-dispersive X-ray spectroscopy (EDX) elemental mapping (Figure 1d–f). A trace (ca. 1.91%) of oxygen was also observed during EDX (Figure S5, Supporting Information) mapping and EDX analysis (Figures S6 and S7, Supporting Information) which plausibly occurred due to slow oxidation of FeSn_2 in air. The chemical composition of the FeSn_2 was analyzed by inductively coupled plasma atomic emission spectroscopy (ICP-AES) that confirmed the one to two

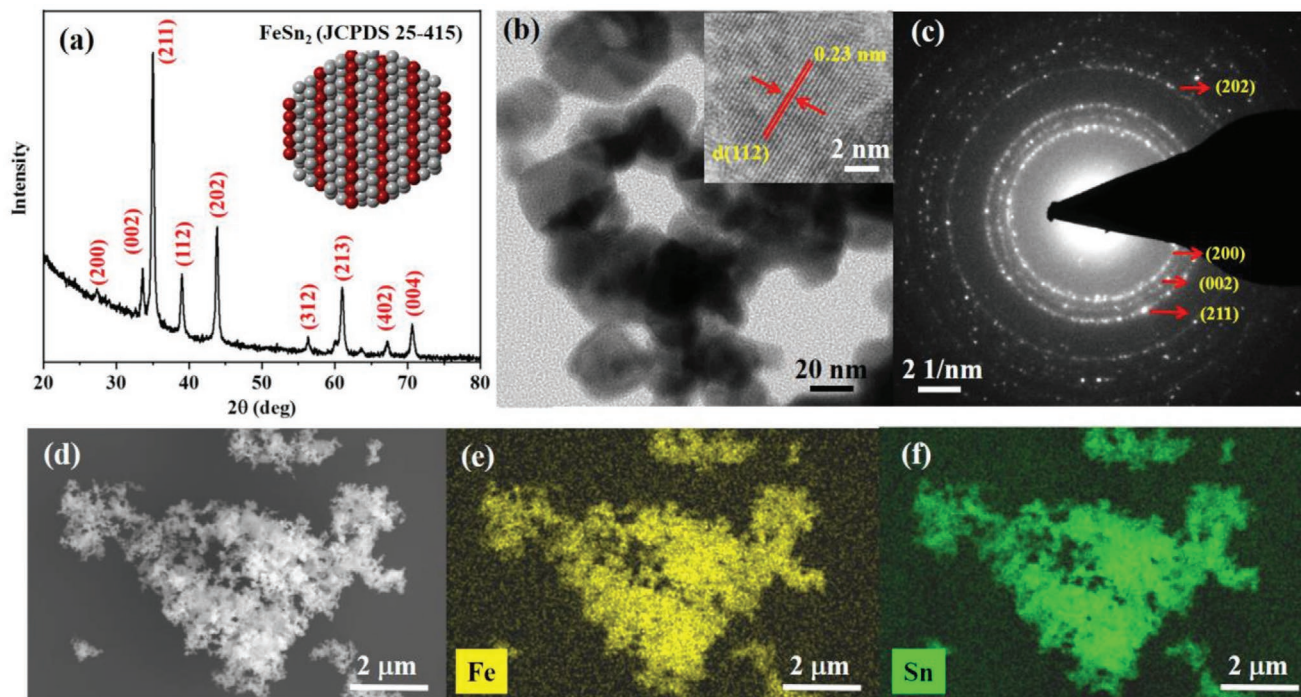


Figure 1. Microscopic analyses of the as-prepared FeSn_2 . a) PXRD pattern of the FeSn_2 with the assignment of diffraction planes according to the reported structure (inset) of FeSn_2 (JCPDS 25-415; Figure S1, Supporting Information). b) The TEM image of FeSn_2 particles and the respective high-resolution image with atomic fringes corresponding to (112) crystal lattice plane with an interplanar spacing of 0.23 nm (b, inset). c) SAED pattern of the nanoparticles displaying diffraction rings to the (200), (002), (211), and (202) corresponding to FeSn_2 . d) SEM image and the elemental mapping of the FeSn_2 displaying the homogenous distribution of Fe. e) and Sn f) shown in yellow and green (oxygen mapping is presented in Figure S5 in the Supporting Information), respectively.

ratio of Fe to Sn (Table S1, Supporting Information). Further, X-ray photoelectron spectroscopy (XPS) was used to investigate the chemical states and the composition of the elements (detailed discussion is given in Figures S8 and S9, Supporting Information). Fe $2p_{3/2}$ and Fe $2p_{1/2}$ displayed two peaks at the binding energies of 707.14 and 720.23 eV, corresponding to Fe⁰ while peaks of Fe^{III} at 710.65 eV (Fe $2p_{3/2}$) and 724.36 eV (Fe $2p_{5/2}$) were also observed resulting from surface passivation of the FeSn₂ (Figure S8, Supporting Information).^[44] Similarly, Sn $3d_{5/2}$ and $3d_{3/2}$ exhibited two sharp peaks at the binding energies of 484.8 and 493.2 eV, which could directly be attributed to the Sn⁰ whereas the peaks at higher binding energies were ascribed to the presence of surface oxidized Sn^{II} (Figure S9, Supporting Information).^[37,44c,45] To establish a direct electrochemical and structure–activity relationship, the metallic Fe phase was synthesized separately (without the Sn precursor) in a similar way as that of FeSn₂ and characterized through PXRD, TEM, high-resolution-TEM, SAED, SEM, EDX, and XPS (Figures S10–S14, Supporting Information).

To evaluate the OER catalytic activity, FeSn₂ was electrophoretically deposited (EPD) on the FTO electrode surface to perform electrochemical measurements in a 1 M KOH aqueous electrolyte in a three-electrode setup. Prior to the electrochemical measurements, the chemical integrity of the FeSn₂ after depositions was confirmed by various methods (Figures S15–20, Supporting Information). In order to have a fair comparison, the metallic Fe, Fe(OH)₃ and α -FeO(OH) were also prepared and electrodeposited with the same mass loading (for synthetic details see the Experimental Section, Figures S10–S14 and Figures S21 and S22, Supporting Information).

Figure 2a shows a typical linear sweep voltammetry (LSV) curve between 1.1 and 1.9 V versus reversible hydrogen electrode (RHE) at a sweep rate of 1 mV s⁻¹. The FeSn₂/FTO electrode delivered a much higher OER current density relative to all other electrodes, indicating the essential role of active Fe sites and conductive Sn sites in the enhancement of the OER catalytic activity. Strikingly, an overpotential of only 273 (\pm 6) mV at a current density of 10 mA cm⁻² was obtained for FeSn₂/FTO electrode, while at the same current density, the Fe/FTO, Fe(OH)₃/FTO and α -FeO(OH)/FTO displayed overpotentials of 480 (\pm 5), 576 (\pm 5), and 620 (\pm 6) mV, respectively. To verify the effect of mass loading and film thickness on the OER activity of the FeSn₂, the electrodeposition time was varied (from 4 to 240 s) which yielded different loadings of the catalyst on the FTO surface (Table S2, Supporting Information). Additionally, polarization curves were recorded with different catalyst loaded films on FTO which also indicated a best OER activity (Figure S23, Supporting Information) for a loading of 0.8 mg FeSn₂ with a thickness of 756 (\pm 0.39) μ m (Figure S24, Supporting Information) with a recorded overpotential 273 (\pm 6) mV at a current density of 10 mA cm⁻² (Figure 3b). It showed an optimum deposition time of 120 s, after which an increase in the mass loading was observed without significant change in the activity (Figure 2b; Table S2, Supporting Information).

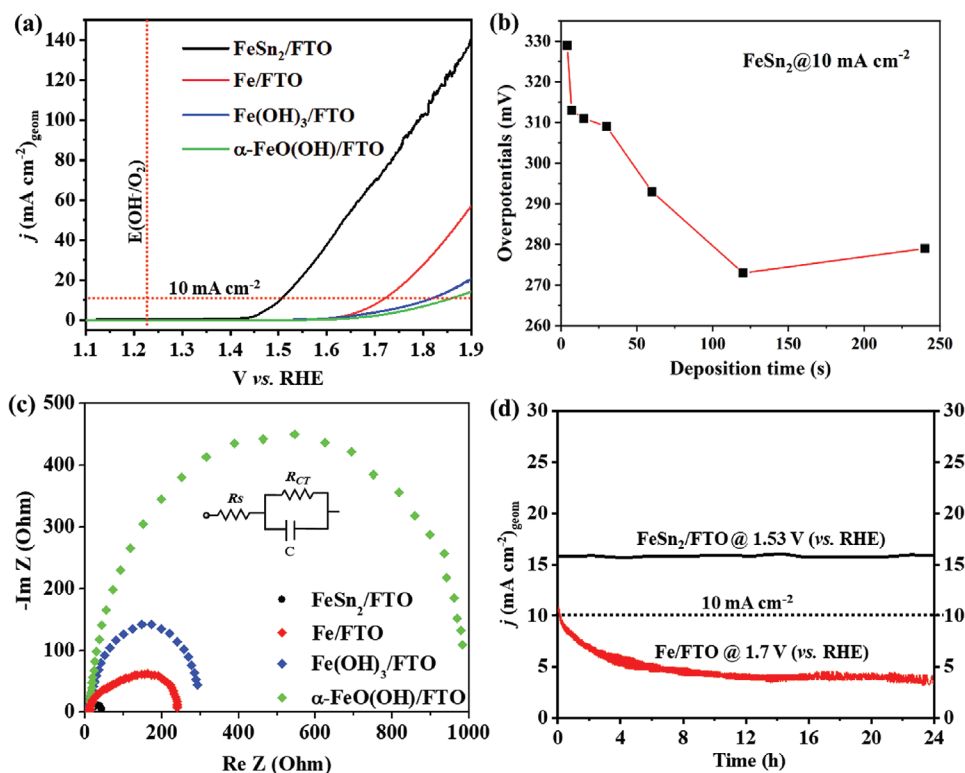


Figure 2. Electrocatalytic OER activity with FeSn₂/FTO in comparison to Fe/FTO, Fe(OH)₃/FTO, and α -FeO(OH)/FTO. a) Polarization curves of FeSn₂/FTO compared to Fe-based reference materials recorded in 1 M KOH solution with a sweep rate of 1 mV s⁻¹. b) The overpotentials of FeSn₂ on 1 cm² FTO surface with respect to deposition time of 4 to 240 s (varying mass loadings; see Table S2 in the Supporting Information). c) Nyquist plots (an equivalent circuit is shown in the inset) at an applied potential of 1.55 V versus RHE. d) chronoamperometric OER studies of FeSn₂/FTO and Fe/FTO at a constant potential of 1.53 and 1.70 V versus RHE, respectively.

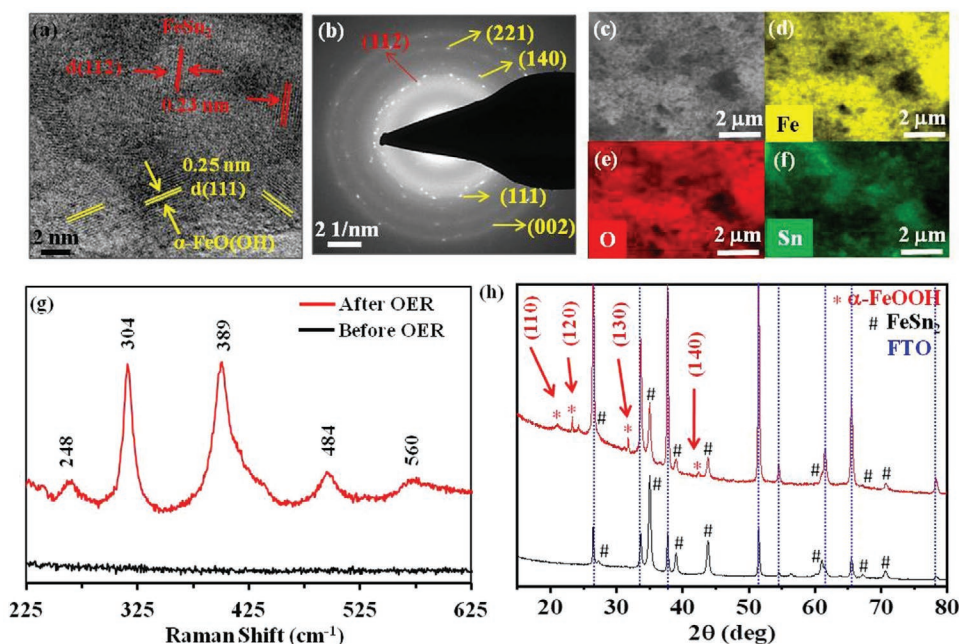


Figure 3. Post OER CA (24 h) analyses of the FeSn₂/FTO. a) The high-resolution TEM image of FeSn₂ showing crystalline fringes of d(111) planes of α -FeO(OH) near the edge of the particle and d(112) planes of FeSn₂ at the core. b) SAED pattern obtained from the area shown in a), exhibiting well-defined rings for FeSn₂ and α -FeO(OH). c–f) SEM image (Figure S30, Supporting Information) and EDX elemental mapping of the FeSn₂/FTO film clearly evidencing the presence of Fe (yellow), O (red), and Sn (green) in the material after catalysis. g) Raman spectra of the FeSn₂/FTO before (black) and after OER CA (red). h) PXRD pattern of the FeSn₂/FTO before (black) and after OER CA (red); the reflections marked by red asterisk (*) can be indexed to (110), (120), (130), and (140) planes of α -FeO(OH) phase (JCPDS 29-713).

The turnover frequency (TOF) as a function of the loading was determined and is also presented in Table S2 in the Supporting Information. The TOF increases with decreased loading revealing that mass/electron transport phenomena are relevant and cause a deviation of a linear relationship between the amount of active sites and the O₂ production rate. Achieved low overpotential with a substantial amount of mass loading indicates the activity is not arisen due to the overloading of the catalysts.^[16d,46] A comparative mass normalized activity and TOF calculated per Fe also showed the remarkable OER activity of FeSn₂ (Figure S25, Supporting Information).^[23a,47] Furthermore, the catalytic OER performance of FeSn₂/FTO was much higher than that of benchmark RuO₂/FTO and IrO₂/FTO catalysts as well as other Fe-based materials reported (Figure S26 and Table S3, Supporting Information).^[16a–c,e,f,j,19a,48] Notably, the LSV curve without *i*R correction gave an overpotential of 316 mV at 10 mA cm⁻² which is also better than previously reported iron-based catalyst (Figure S27 and Table S3, Supporting Information).^[49]

The catalytic OER kinetics of the presented catalysts is evaluated by the Tafel plots. A Tafel slope of 33 (\pm 2) mV dec⁻¹ was determined for FeSn₂/FTO, which is comparable to those of the state-of-the-art benchmark Fe-based catalysts (Figure 2b; Figure S28, Supporting Information), suggesting facile electron transfer with intermetallic FeSn₂.^[49] A semicircular Nyquist plot obtained from electrochemical impedance spectroscopy (EIS) measurements with FeSn₂ indicated a favorable charge transfer between electrolyte and electrode interface with a low charge transfer resistance (*R*_{CT}) (Figure 2c; Table S4, Supporting Information).^[50] As expected, the *R*_{CT} values of the presented catalysts

are in accordance with the corresponding electrocatalytic OER activity. Apart from low overpotentials, which determine the efficiency of a catalyst, stability is another crucial factor to evaluate its practical implication. Under a chronoamperometric OER condition (OER CA), the FeSn₂/FTO catalyst remained stable with a current density above 15 mA cm⁻² by an applied potential of 1.53 V versus RHE (at an overpotential of 300 mV) (Figure 2d). However, a significant drop in the current was observed (up to 61%), when metallic Fe/FTO film was applied under similar OER CA conditions at 1.7 V versus RHE (the necessary potential to reach 10 mA cm⁻²) making it an unsuitable anode material most likely due to the low electrical conductivity less abundant surface active sites compared to FeSn₂ (Figure 2d).

Dynamic restructuring of the (pre)catalyst under alkaline electrocatalytic (OER CA) conditions has recently been studied systematically to reveal the bulk and surface-active species of the materials and to understand their reaction pathways.^[12,23e,51] Therefore, to further investigate the reason for the better electrochemical characteristics of FeSn₂ over other catalysts, we examined the FeSn₂/FTO films after OER CA conditions. Foremost, ICP-AES revealed a substantial loss of Sn (\approx 30%) suggesting that FeSn₂ is indeed an electro(pre) catalyst that undergoes a structural transformation during the electrocatalytic OER condition. High-resolution TEM images showed a crystalline core of FeSn₂ surrounded by the crystalline α -FeO(OH) layer. The two phases could be differentiated by the d(112) planes of FeSn₂ (JCPDS 25-415) and d(111) planes of α -FeO(OH) (JCPDS 29-713) near the edge of on an individual particle (Figure 3a; Figure S29, Supporting Information).^[16h] Furthermore, the SAED pattern depicts the well-defined rings

of both FeSn_2 and $\alpha\text{-FeO(OH)}$ (Figure 3b). The SEM image of FeSn_2 (Figure 3c) after OER CA displayed noticeable morphological changes during the electrochemical performance (Figure S30, Supporting Information). The elemental mapping and EDX (Figure 3d–f; Figure S31, Supporting Information) of the film confirmed the incorporation of an enormous amount of oxygen into the surface of FeSn_2 which further validates the formation of $\alpha\text{-FeO(OH)}$. Raman spectroscopy, a very sensitive probe to surface structure, was also conducted to unveil the surface structure of FeSn_2 before and after OER electrocatalysis (Figure 3g). The spectrum shows Raman vibrations at 248 (w), 304 (s), 389 (s), 484 (w) and 560 (w) cm^{-1} which are in good agreement with the reported vibrations of pure phase goethite, $\alpha\text{-FeO(OH)}$ ^[52] whereas the Raman spectrum of FeSn_2 does not possess any peaks (Figure 3g; Figure S32, Supporting Information). Further analysis of the film by PXRD after OER CA resulted in sharp reflections for $\alpha\text{-FeO(OH)}$ along with the diffractions for FeSn_2 (Figure 3h). Additional evidence for the formation of $\alpha\text{-FeO(OH)}@ \text{FeSn}_2$ under electrocatalytic condition, via surface restructuring, was provided by XPS. The Fe 2p XPS spectrum reveals that Fe^{III} is the dominant species (Figure S33a, Supporting Information)^[44] while a weak and broad peak corresponding to Fe^0 was still retained at the FeSn_2 surface after OER. The Sn 3p and Sn 3d XPS spectra also exhibited oxidized Sn species on the surface of the film owing to the trapping of oxidized species from the electrolyte and are consistent with literature reports (Figure S33a,b, Supporting Information).^[37,44c,45] Likewise, the peaks in the O 1s XPS spectrum also support the presence of -OH^- and $\text{O}^{\text{-II}}$ species on the surface after OER (Figure S33c, Supporting Information). Overall, the above results evidence the formation of a reactive $\alpha\text{-FeO(OH)}$ overlayer at the surface of the highly conducting FeSn_2 core to achieve efficient OER.

To get additional insight into the reasons for the improved electrocatalytic performance of FeSn_2 among the other Fe-based catalysts, we performed ex situ four-point probe resistivity measurements of the thin films. The as-deposited FeSn_2/FTO thin film had a resistivity of $29 \times 10^1 \Omega \text{ cm}$. The resistivity of the surface oxidized, as deposited Fe/FTO had a three to four magnitudes higher resistivity whereas much higher values were found for $\text{Fe(OH)}_3/\text{FTO}$ and $\alpha\text{-FeO(OH)}/\text{FTO}$ (Table S5, Supporting Information). Surprisingly, $\alpha\text{-FeO(OH)}@ \text{FeSn}_2/\text{FTO}$ film was still dramatically more conducting than the oxidized iron compounds (Table S5, Supporting Information). It should be noted that the ex situ conductivity measurements are not necessarily able to predict the electron transport abilities of materials under OER conditions.^[53] Nevertheless, conductivity limitations of FeO(OH) are reported in the literature even at OER conditions,^[19a] and the herein performed conductivity measurement proves that the remaining FeSn_2 can dramatically reduce these limitations even without an applied potential. Furthermore, the electrocatalytic activity of FeO(OH) is a strong function of the underlying substrate and the synergistic interaction of Au/AuO_x with FeO(OH) can strongly increase its OER performance.^[19a,54] For $\alpha\text{-FeO(OH)}@ \text{FeSn}_2$, a similar synergistic effect at the interface between the metallic phase containing the heavy nucleus Sn and $\alpha\text{-FeO(OH)}$ might be present. However, detailed theoretical investigations are needed to prove this hypothesis. Additionally, chemisorb water is suspected

to block the active iron sites from reactive hydroxide in FeO(OH) .^[52c] Such chemisorbed water could also be detected in high vacuum XPS measurements. In the case of $\alpha\text{-FeO(OH)}@ \text{FeSn}_2$, no chemisorbed water is present in the O 1s XPS indicating good active site availability.

Most importantly, no decrease in the OER activity or leaching of iron from FeSn_2 under CA could be observed in our case. One reason for this is the low operation potential that is required to achieve the OER. For amorphous FeO(OH) , iron leaches relatively fast at an overpotential of 450 mV, but significantly slower already at an overpotential of 350 mV.^[19a] Furthermore, it was recently shown that crystalline $\alpha\text{-FeO(OH)}$, in contrast to amorphous phases, is stable under OER conditions and can resist solvation at overpotentials as high as 800 mV.^[52c] In the same report, a comparable activity of crystalline $\alpha\text{-FeO(OH)}$ and the amorphous $\gamma\text{-FeO(OH)}$ phase was revealed. This shows that crystalline phase $\alpha\text{-FeO(OH)}$ can combine a high activity with a good stability, in contrast to previous reports where amorphous phases are usually considered to be more active.^[55]

After the successful demonstration of FeSn_2/FTO as a high-performance electrocatalyst, we deposited the same catalysts on 3D-interconnected porous and conducting NF, without altering its chemical integrity (Figures S34–S36, Supporting Information). The electrocatalytic study was then investigated with respect to the OER in 1 M KOH aqueous electrolyte. Figure 4a exhibits representative LSV curves of various Fe-based catalysts on NF at a scan rate of 1 mV s^{-1} , along with bare NF as a reference. Similar to FTO deposited substrates, FeSn_2/NF displayed an exceptionally small overpotential value of $197 \pm 4 \text{ mV}$ at a current density of 10 mA cm^{-2} and reached an extremely high catalytic current density of 500 mA cm^{-2} at an electrode potential of 1.56 V (vs RHE) whereas the catalysts Fe/NF , $\text{Fe(OH)}_3/\text{NF}$, $\alpha\text{-FeO(OH)}/\text{NF}$ and bare NF displayed poor catalytic OER activity. Moreover, the overpotential recorded for the FeSn_2/NF electrocatalyst not only supersedes the state-of-the-art noble metal catalysts, RuO_2/NF and IrO_2/NF (Figure S37, Supporting Information), but this value is significantly lower (33 mV) than that reported analogous intermetallic phase CoSn_2 ($230 \text{ mV @ } 10 \text{ mA cm}^{-2}$) (Figure 4b; Table S3, Supporting Information) and other Fe, Fe–Ni- and Fe–Co-based electrocatalysts (Table S3, Supporting Information).^[56] The recorded overpotential of FeSn_2 is even ca. 130 mV less than the 2D nanoplate FeSe_2 catalysts.^[57] Notably, an LSV curve without iR correction yielded an overpotential of 209 mV at 10 mA cm^{-2} (Figure S38, Supporting Information). The Tafel slope calculated for FeSn_2 was $31 \pm 1 \text{ mV dec}^{-1}$, which is comparable to the other Fe-based catalysts (Figure 4c; Figure S39, Supporting Information).^[49] FeSn_2/NF showed a significantly lower R_{CT} (Figure 4d; Figure S40, Supporting Information) than other electrodes, which highlights rapid charge transfer kinetics at the solution–electrode interface of FeSn_2 (Table S6, Supporting Information).^[50a] A detailed analysis was performed to ensure that the higher electrochemical surface area (ECSA) is most plausibly one of the controlling factors to obtain the better electrochemical performance of the FeSn_2/NF . The calculated double-layer capacitance (C_{dl}) and the estimated ECSA^[58] of FeSn_2 , and other iron-based catalyst is summarized in Figure S41 in the Supporting Information, which confirmed a C_{dl} of 0.85 mF cm^{-2} and an ECSA of 0.49 cm^2 for FeSn_2 electro(pre)catalyst.^[9b,16f,37,51b,59] The

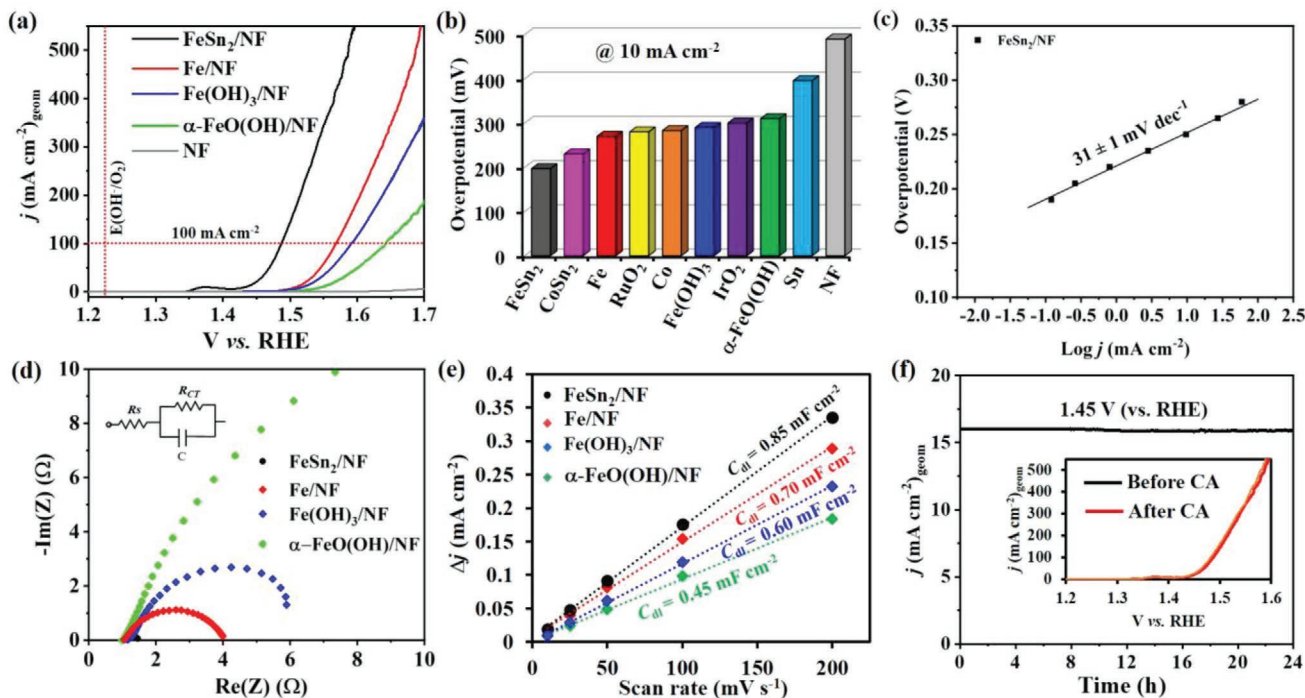


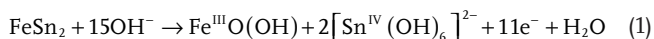
Figure 4. Electrocatalytic OER with FeSn₂/NF in comparison to Fe/NF, Fe(OH)₃/NF and α -FeO(OH)/NF. a) Polarization curves of the OER recorded in 1 M KOH solution with a sweep rate of 1 mV s⁻¹ b) Comparison of the overpotential recorded at 10 mA cm⁻² presented materials with respect to the RuO₂/NF and IrO₂/NF and recently reported CoSn₂/NF, Co, and Sn. c) Tafel slope of FeSn₂/NF calculated by the steady-state method. d) Nyquist plots of Fe based materials at an applied potential of 1.55 V versus RHE. e) C_{dl} values of the materials calculated from the slopes of the linear fitting of Δj (mA cm⁻²) versus scan rate (mV s⁻¹) (Figure S41, Supporting Information). f) Long-term stability experiment of FeSn₂/NF at 1.45 V versus RHE and the inset shows LSV curves before (black) and after OER (red).

ECSA normalized electrocatalytic OER activity of the materials shows that the highest activity is achieved with FeSn₂ (Figure S42, Supporting Information). The Brunauer–Emmet–Teller (BET) surface areas of the materials have been also determined (Table S7, Supporting Information), and consequently, the normalization of the activities by these values confirms the best activity of FeSn₂ among the other iron-based catalysts tested herein (Figure S43, Supporting Information).

The FeSn₂/NF sustained for 24 h under an electrochemical OER CA condition with a subtle change in current density, very similar to that observed for the OER CA with FeSn₂/FTO (Figure 4f). The LSV curves recorded after OER CA (24 h) showed almost unchanged overpotentials at 10 mA cm⁻² (Figure 4f, inset). Post catalytic analyses of FeSn₂/NF after OER CA also indicated the formation of α -FeO(OH) layer covering the surface of FeSn₂ (Figures S44 and S45, Supporting Information) and is consistent with surface rearrangements observed on FeSn₂/FTO (Figure 3). ICP-AES analysis suggests the spontaneous dissolution of Sn from the catalyst's surface. The loss of Sn continues with the progress of OER CA and then probably ends after a certain ratio, as the electrolyte cannot penetrate to the FeSn₂ core anymore forming a stable FeO(OH)@FeSn₂. After 60 h of continuous electrolysis (OER CA) at 220 mV overpotential, ICP-AES analysis of the electrolyte shows that approximately 40% of the Sn leaches out to the electrolyte solution. A comparatively stable current density was observed throughout the OER CA measurement (Figure S46, Supporting Information). The iron content in the electrolyte was not significantly

above the detection limit of the ICP-AES analysis. The C_{dl} and ECSA measured post-OER catalysis showed a slight enhancement that could be attributed to the initial surface conversion of the FeSn₂ (Figure S47, Supporting Information), suggesting a disordered α -FeO(OH) surface. Moreover, such rigorous surface modulation/restructuring to form active surface stabilized Fe(OH)₂/FeO(OH) electrodes under OER conditions have recently been realized for Fe-based chalcogenides and pnictides.^[9b,16c,e,f]

A plausible pathway of α -FeO(OH) formation on the FeSn₂ surface can be explained via oxidative leaching of Sn, and subsequent oxidation of iron site.^[60] As suggested by the Pourbaix diagrams, during the alkaline OER, a reactive Fe^{II}(OH)₂ may form via oxidation of Fe^{δ+} to Fe^{II} and that finally transforms to α -Fe(O)OH (Equation (1)) under applied potentials (note that at higher anodic applied potentials, the transformation of FeO(OH) into soluble (FeO₄)²⁻ is inevitable).^[61]



It could be anticipated that a higher degree of structural ordering of FeSn₂ core allows a regular arrangement of Fe(O)OH which essentially leads to a crystalline nature of the Fe(O)OH. The conversion ratio of FeSn₂ to α -FeO(OH) is strictly controlled by the dissolution rate of Sn and duration of OER. This was further confirmed by ratios obtained from the EDX and ICP-AES analysis after the long-term stability tests of 24 and 60 h.

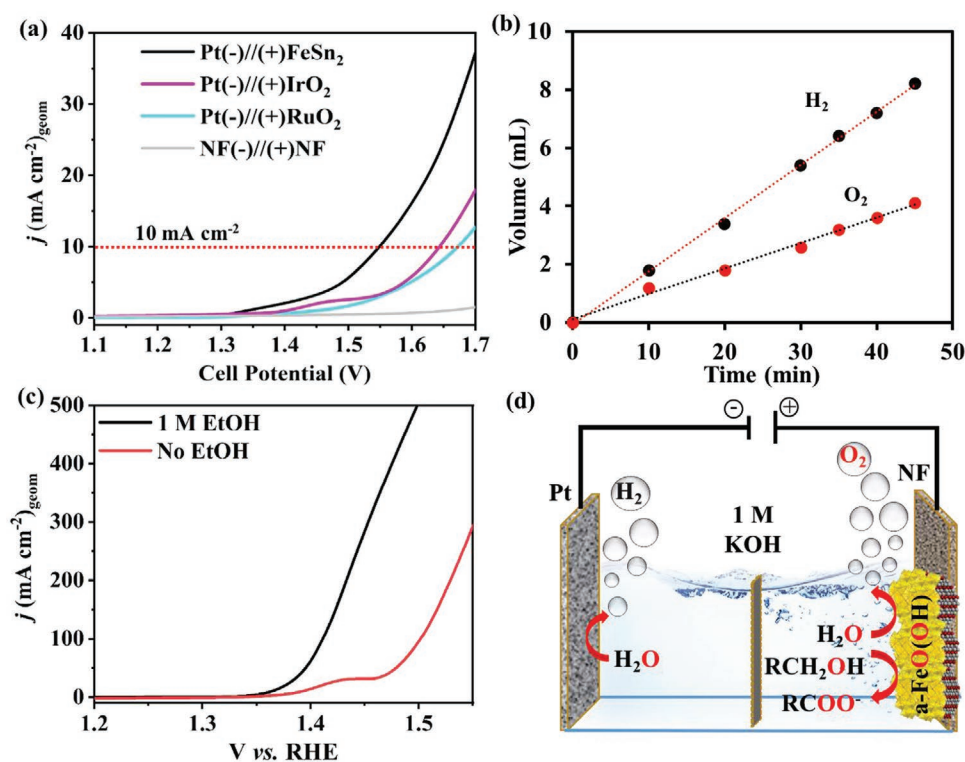


Figure 5. The FeSn₂/NF anodes for electrocatalytic water splitting and organic oxidation. a) Polarization curves measured for Pt(-)/(+)FeSn₂/NF, Pt(-)/(+)IrO₂/NF, Pt(-)/(+)RuO₂/NF and NF(-)/(+)NF. b) Evolution of stoichiometric amount of H₂ and O₂ (2:1) during electrolysis. c) Polarization curves recorded in a three-electrode set-up with FeSn₂/NF as a working electrode in aqueous 1 M KOH in the absence and presence of 1 M ethanol (sweep rate; 5 mV s⁻¹). d) Schematic representation of water electrolysis and electrocatalytic oxidation of alcohols with FeSn₂/NF as anode and Pt as the cathode (in a divided cell).

To prove that the OER activity of FeSn₂ is superior to the state-of-the-art NiFe-based catalysts,^[24b,c,25a,26b,62] we additionally synthesized a highly active FeNi₂O₄ phase (see synthesis, Figure S48, Supporting Information). The FeNi₂O₄ was electrodeposited on both FTO and NF and measured in alkaline electrolyte, similar to that of FeSn₂. The overpotentials of FeNi₂O₄/FTO and FeNi₂O₄/NF attained at a current density of 10 mA cm⁻² were 334 and 230 mV, respectively (Figure S49, Supporting Information), which are surprisingly higher than the presented FeSn₂ catalysts. This indeed demonstrates the essential role of Fe as an active site and Sn as a conductive element in enhancing the overall catalytic efficiency, without the introduction of a second transition metal as reported for NiFe-based materials.^[24b,c,25a,26b,48d,62]

As it was proven that FeSn₂/NF can be a competitive anode for the OER, a two-electrode set-up was fabricated to carry out the reaction of overall water-splitting using a Pt cathode coupled to FeSn₂/NF anode (Pt(-)/(+)FeSn₂/NF) in alkaline electrolyte. Remarkably, the Pt(-)/(+)FeSn₂/NF exhibited an extremely reduced cell potential of 1.53 V at 10 mA cm⁻², which was much lower than cell constructed with Pt(-)/(+)RuO₂/NF (1.64 V) and Pt(-)/(+)IrO₂/NF (1.66 V) (Figure 5a) emphasizing the prominence of an active and conductive anode for durable water electrolysis. The long-term alkaline water electrolysis of Pt(-)/(+)FeSn₂/NF was conducted at a cell potential of 1.53 V that showed notable sustainability of the system under a longer run (Figure S50, Supporting

Information). In an inverted closed-cell (Figure S51, Supporting Information), using Pt(-)/(+)FeSn₂/NF as a pair of working electrodes, the volumes of the evolved gases in both compartments were subsequently recorded and the ratio of produced H₂ and O₂ overtime was about 2:1, which matches perfectly with the theoretically predicted water splitting ratio (Figure 5b). The Faradaic efficiency (FE) of the overall water splitting was further calculated (in a separate experiment) using gas chromatography (GC) and a FE of ≈94% was achieved for OER (FeSn₂/NF) and 97% for HER (Pt) (see details in the Supporting Information and Table S8, Supporting Information).

Recently, the transition metal-based catalysts have gained immense interest in the oxidation of important organic substrates, including the most important substrates such as HMF, ethanol, and acetaldehyde.^[31c,e,32a] The utilization of electrooxidation opens a new scope to avoid the use of toxic oxidants and harsh reaction conditions for the electrosynthesis of value-added organic products in a green and effective approach.^[29] In addition to that, electrocatalytic alcohol oxidation has a broad context to develop direct alcohol fuel cells (DAFCs) and it has been well-studied with noble metal (Pt, Pd, and Au) based electrodes,^[32b] whereas, the practical application of non-noble anodes is still limited. Inspired by the promising OER activity of FeSn₂/NF, the catalytic efficiency of this electro(pre)catalyst was used for the electrooxidation of ethanol, carboxaldehyde, and HMF.

The electrocatalytic oxidation of ethanol was tested in aqueous 1 M KOH using a three-electrode set-up in a similar

fashion to that of OER. Polarization curves obtained from the LSV measurement showed a rapid increment in current density beyond 1.35 V (vs RHE) when a mixture of 1 M KOH and 1 M ethanol was used as electrolyte solution (Figure 5c). However, in the absence of 1 M ethanol in the electrolyte (only 1 M KOH), the LSV curve showed only the OER and revealed that the oxidation of ethanol transpired significantly lower potentials than that of OER. This study suggests that the Fe⁰ in FeSn₂ oxidizes to form higher-valent Fe species which spontaneously oxidize ethanol in comparison to that of alkaline water. In order to comprehend the outcome of ethanol after electrooxidation, a customized two-compartment divided cell set-up was fabricated using FeSn₂/NF as anode and Pt as the cathode (Figure 5d). At a constant current of 10 mA cm⁻², the ethanol converted into acetic acid as the sole four-electron oxidized product (–CH₂OH to –COOH; 4 e⁻ oxidation) at the anode, as identified and quantified by ¹H NMR (Figures S52 and S53, Supporting Information) and at the cathode, a continuous H₂ production was observed. The achieved FE of ethanol to acetic acid conversion (at the anode) is ≈90% after 2 h of applied current implying a potency of the Pt(-)/(+)FeSn₂/NF cell. Similar to ethanol oxidation, the two-electrode set-up was also constructed to electrooxidize acetaldehyde to acetic acid and ≈85% FE was also achieved at a constant current of 10 mA cm⁻² (Figure S54, Supporting Information). In fact, the acetic acid (CH₃COOH), the oxidation product of C₂H₅OH and CH₃CHO, is a high boiling polar solvent used in common practice for standard organic synthesis. Besides, a paired C₂H₅OH oxidation with simultaneous H₂ formation are two important steps that occur in direct ethanol fuel cell and FeSn₂/NF anode with 90% efficiency. This system would be a potential alternative to the noble metal anodes traditionally used to achieve the highest efficiency.

The electrosynthesis of FDCA from HMF oxidation is a value-added component for polymer manufacturing, and polyester synthesis, for instance, polyethylene 2,5-furandicarboxylate (PEF) and polyethylene terephthalate.^[29] HMF contains a dual functionality; –CHO and –CH₂OH and using FeSn₂/NF as the anode, electrolysis for 2 h in an alkaline solution (1 M KOH) containing 20 × 10⁻³ M of HMF, FDCA was obtained as the only oxidation product (Figures S55 and S56, Supporting Information) with a FE of ≈90%. Interestingly, the FE for all multistep electrocatalytic oxidation reactions (Schemes S1 and S2, Supporting Information), acetic acid from ethanol (4 e⁻), from acetaldehyde (2 e⁻) and HMF to FDCA (6 e⁻), is extremely high in comparison to the literature reports and are in the range of 85–90%, indicating superior efficiency.^[36–38] This study shows the use of ordered intermetallic FeSn₂ for the first time for the electrooxidation of organics of value-added chemicals as well as OER.

In summary, we report a straightforward synthetic strategy to isolate a highly crystalline intermetallic FeSn₂ nanoparticles, avoiding traditional high-temperature solid-state techniques. While deposited on electrode substrates, FeSn₂ behaves as a potential anode material for electrocatalytic OER with a substantially low overpotential of 273 mV on the FTO surface and 197 mV on NF (at 10 mA cm⁻²), surpassing the previously reported pure iron-based materials for OER. The superior activity of the FeSn₂ catalyst is most

likely due to higher electron conductivity within the structurally ordered metallic nanostructure compared to other iron-based catalysts reported earlier and/or tested herein, as evident by comparatively low resistances obtained from the four-point probe resistivity measurements. Detailed microscopic and spectroscopic postanalyses indicate the formation of a crystalline α-FeO(OH) (goethite) as an overlayer via a surface restructuring to act as an active species for OER on the surface of highly conducting FeSn₂. Utilization of this intermetallic FeSn₂ nanostructure using Fe, one of the most earth-abundant metals, as the active site to form the surface-active α-FeO(OH) species and FeSn₂ at the core as a conductive site is found to be beneficial compared to earlier strategies to improve the poor conductivity of iron-based materials by doping with one or two additional transition metal (Ni/Co) and/or varying different conductive substrates. The superior OER performance of this in situ generated α-FeO(OH)@FeSn₂ catalyst provides an additional opportunity to construct a reliable overall water splitting cell Pt(-)/(+)FeSn₂/NF with a cell potential of 1.53 V. We further utilized the nonprecious α-FeO(OH)@FeSn₂ anode for the electrosynthesis of two valuable organic compounds acetic acid and FDCA starting from ethanol/acetaldehyde and HMF, respectively, with highest FE. The findings obtained here are vital steps forward in the direction of the rational design of low-cost electrodes for future electrochemical systems involving multiple applications such as OER, water electrolysis, and green chemical synthesis.

Supporting Information

Supporting Information is available from the Wiley Online Library or from the author.

Acknowledgements

B.C. and R.B.-S. contributed equally to this work. The work is funded by the Deutsche Forschungsgemeinschaft (DFG, German Research Foundation) under Germany's Excellence Strategy—EXC 2008—390540038—UniSysCat. The authors are also indebted to Dr. Vitaly Gutkin for XPS measurement and to Dr. Stefan Berendts, Eva Maria Heppke, and Ina Speckmann (AK Lerch, TU Berlin) for PXRD measurements, and Konstantin Laun (AK Hildebrandt) for Raman measurements.

Conflict of Interest

The authors declare no conflict of interest.

Keywords

iron stannides, overall water splitting, oxygenation, oxyhydroxides, water oxidation

Received: April 21, 2020

Revised: June 8, 2020

Published online: June 24, 2020

- [1] a) J. Qi, W. Zhang, R. Cao, *Adv. Energy Mater.* **2018**, *8*, 1701620; b) Y. Wang, H. Suzuki, J. Xie, O. Tomita, D. J. Martin, M. Higashi, D. Kong, R. Abe, J. Tang, *Chem. Rev.* **2018**, *118*, 5201; c) H. B. Gray, *Nat. Chem.* **2009**, *1*, 7; d) T. A. Faunce, W. Lubitz, A. W. Rutherford, D. MacFarlane, G. F. Moore, P. Yang, D. G. Nocera, T. A. Moore, D. H. Gregory, S. Fukuzumi, K. B. Yoon, F. A. Armstrong, M. R. Wasielewski, S. Styring, *Energy Environ. Sci.* **2013**, *6*, 695; e) C. Panda, P. W. Menezes, S. L. Yao, J. Schmidt, C. Walter, J. N. Hausmann, M. Driess, *J. Am. Chem. Soc.* **2019**, *141*, 13306.
- [2] a) T. J. Meyer, M. V. Sheridan, B. D. Sherman, *Chem. Soc. Rev.* **2017**, *46*, 6148; b) D. A. Pantazis, *ACS Catal.* **2018**, *8*, 9477; c) C. Panda, P. W. Menezes, M. Driess, *Angew. Chem., Int. Ed.* **2018**, *57*, 11130.
- [3] B. You, Y. Sun, *Acc. Chem. Res.* **2018**, *51*, 1571.
- [4] a) J. H. Montoya, L. C. Seitz, P. Chakthranont, A. Vojvodic, T. F. Jaramillo, J. K. Nørskov, *Nat. Mater.* **2017**, *16*, 70; b) B. M. Hunter, H. B. Gray, A. M. Müller, *Chem. Rev.* **2016**, *116*, 14120.
- [5] a) Y. Jiao, Y. Zheng, M. Jaroniec, S. Z. Qiao, *Chem. Soc. Rev.* **2015**, *44*, 2060; b) I. Roger, M. A. Shipman, M. D. Symes, *Nat. Rev. Chem.* **2017**, *1*, 928; c) C. C. L. McCrory, S. Jung, I. M. Ferrer, S. M. Chatman, J. C. Peters, T. F. Jaramillo, *J. Am. Chem. Soc.* **2015**, *137*, 4347; d) R. Gao, D. Yan, *Adv. Energy Mater.* **2020**, *10*, 1900954.
- [6] a) F. Song, L. Bai, A. Moysiadou, S. Lee, C. Hu, L. Liardet, X. Hu, *J. Am. Chem. Soc.* **2018**, *140*, 7748; b) B. Chakraborty, A. Indra, P. V. Menezes, M. Driess, P. W. Menezes, *Mater. Today Chem.* **2020**, *15*, 100226.
- [7] M. W. Kanan, Y. Surendranath, D. G. Nocera, *Chem. Soc. Rev.* **2009**, *38*, 109.
- [8] a) Y. Guo, T. Park, J. W. Yi, J. Henzie, J. Kim, Z. Wang, B. Jiang, Y. Bando, Y. Sugahara, J. Tang, Y. Yamauchi, *Adv. Mater.* **2019**, *31*, 1807134; b) S. Anantharaj, S. R. Ede, K. Sakthikumar, K. Karthick, S. Mishra, S. Kundu, *ACS Catal.* **2016**, *6*, 8069; c) B. Chakraborty, S. Kalra, R. Beltran-Suito, C. Das, T. Hellmann, P. W. Menezes, M. Driess, *Chem. - Asian J.* **2020**, *15*, 852; d) B. Chakraborty, R. Beltran-Suito, V. Hlulkhy, J. Schmidt, P. W. Menezes, M. Driess, *ChemSusChem* **2020**, <https://doi.org/10.1002/cssc.202000445>; e) J. N. Hausmann, E. M. Heppke, R. Beltran-Suito, J. Schmidt, M. Muhlbauer, M. Lerch, P. W. Menezes, M. Driess, *ChemCatChem* **2020**, *12*, 1161.
- [9] a) K. N. Dinh, Q. Liang, C.-F. Du, J. Zhao, A. I. Y. Tok, H. Mao, Q. Yan, *Nano Today* **2019**, *25*, 99; b) B. R. Wygant, K. Kawashima, C. B. Mullins, *ACS Energy Lett.* **2018**, *3*, 2956.
- [10] S. Gupta, M. K. Patel, A. Miotello, N. Patel, *Adv. Funct. Mater.* **2020**, *30*, 1906481.
- [11] P. W. Menezes, C. Panda, S. Loos, F. Bunschei-Bruns, C. Walter, M. Schwarze, X. Deng, H. Dau, M. Driess, *Energy Environ. Sci.* **2018**, *11*, 1287.
- [12] P. W. Menezes, A. Indra, I. Zaharieva, C. Walter, S. Loos, S. Hoffmann, R. Schlögl, H. Dau, M. Driess, *Energy Environ. Sci.* **2019**, *12*, 988.
- [13] H. E. Suess, H. C. Urey, *Rev. Mod. Phys.* **1956**, *28*, 53.
- [14] V. Abbate, R. Hider, *Metallomics* **2017**, *9*, 1467.
- [15] a) S. Liu, L. Zheng, P. Yu, S. Han, X. Fang, *Adv. Funct. Mater.* **2016**, *26*, 3331; b) S. Han, L. Hu, Z. Liang, S. Wageh, A. A. Al-Ghamdi, Y. Chen, X. Fang, *Adv. Funct. Mater.* **2014**, *24*, 5719.
- [16] a) S. Chen, Z. Kang, X. Zhang, J. Xie, H. Wang, W. Shao, X. Zheng, W. Yan, B. Pan, Y. Xie, *ACS Cent. Sci.* **2017**, *3*, 1221; b) L. Yang, Z. Guo, J. Huang, Y. Xi, R. Gao, G. Su, W. Wang, L. Cao, B. Dong, *Adv. Mater.* **2017**, *29*, 1704574; c) H. Li, P. Wen, Q. Li, C. Dun, J. Xing, C. Lu, S. Adhikari, L. Jiang, D. L. Carroll, S. M. Geyer, *Adv. Energy Mater.* **2017**, *7*, 1700513; d) F. Yu, H. Zhou, Z. Zhu, J. Sun, R. He, J. Bao, S. Chen, Z. Ren, *ACS Catal.* **2017**, *7*, 2052; e) C. Panda, P. W. Menezes, C. Walter, S. Yao, M. E. Miehlich, V. Gutkin, K. Meyer, M. Driess, *Angew. Chem., Int. Ed.* **2017**, *56*, 10506; f) S. Yao, V. Forstner, P. W. Menezes, C. Panda, S. Mebs, E. M. Zolnhofer, M. E. Miehlich, T. Szilvási, N. Ashok Kumar, M. Haumann, K. Meyer, H. Grützmacher, M. Driess, *Chem. Sci.* **2018**, *9*, 8590; g) H. Bandal, K. K. Reddy, A. Chaugule, H. Kim, *J. Power Sources* **2018**, *395*, 106; h) J. Hu, S. Li, J. Chu, S. Niu, J. Wang, Y. Du, Z. Li, X. Han, P. Xu, *ACS Catal.* **2019**, *9*, 10705; i) X. Zou, Y. Wu, Y. Liu, D. Liu, W. Li, L. Gu, H. Liu, P. Wang, L. Sun, Y. Zhang, *Chem* **2018**, *4*, 1139; j) Y. Wu, M. Chen, Y. Han, H. Luo, X. Su, M.-T. Zhang, X. Lin, J. Sun, L. Wang, L. Deng, W. Zhang, R. Cao, *Angew. Chem., Int. Ed.* **2015**, *54*, 4870; k) S. Han, X. Hu, J. Wang, X. Fang, Y. Zhu, *Adv. Energy Mater.* **2018**, *8*, 1800955.
- [17] a) M. Arif, G. Yasin, M. Shakeel, M. A. Mushtaq, W. Ye, X. Fang, S. Ji, D. Yan, *Mater. Chem. Front.* **2019**, *3*, 520; b) R. Gao, D. Yan, *Nano Res.* **2018**, *11*, 1883.
- [18] M. Arif, G. Yasin, L. Luo, W. Ye, M. A. Mushtaq, X. Fang, X. Xiang, S. Ji, D. Yan, *Appl. Catal., B* **2020**, *265*, 118559.
- [19] a) S. Zou, M. S. Burke, M. G. Kast, J. Fan, N. Danilovic, S. W. Boettcher, *Chem. Mater.* **2015**, *27*, 8011; b) K. Klykyn, K. M. Rosso, V. Alexandrov, *J. Phys. Chem. C* **2018**, *122*, 16086.
- [20] R. Subbaraman, D. Tripkovic, K.-C. Chang, D. Strmcnik, A. P. Paulikas, P. Hirunsit, M. Chan, J. Greeley, V. Stamenkovic, N. M. Markovic, *Nat. Mater.* **2012**, *11*, 550.
- [21] a) A. S. Batchellor, S. W. Boettcher, *ACS Catal.* **2015**, *5*, 6680; b) L. Trotochaud, S. L. Young, J. K. Ranney, S. W. Boettcher, *J. Am. Chem. Soc.* **2014**, *136*, 6744; c) D. Friebe, M. W. Louie, M. Bajdich, K. E. Sanwald, Y. Cai, A. M. Wise, M.-J. Cheng, D. Sokaras, T.-C. Weng, R. Alonso-Mori, R. C. Davis, J. R. Bargar, J. K. Nørskov, A. Nilsson, A. T. Bell, *J. Am. Chem. Soc.* **2015**, *137*, 1305.
- [22] a) C. G. Morales-Guio, L. Liardet, X. Hu, *J. Am. Chem. Soc.* **2016**, *138*, 8946; b) M. S. Burke, S. Zou, L. J. Enman, J. E. Kellon, C. A. Gabor, E. Pledger, S. W. Boettcher, *J. Phys. Chem. Lett.* **2015**, *6*, 3737; c) M. S. Burke, L. J. Enman, A. S. Batchellor, S. Zou, S. W. Boettcher, *Chem. Mater.* **2015**, *27*, 7549; d) L. Bai, C.-S. Hsu, D. T. L. Alexander, H. M. Chen, X. Hu, *J. Am. Chem. Soc.* **2019**, *141*, 14190.
- [23] a) C. Roy, B. Sebok, S. B. Scott, E. M. Fiordaliso, J. E. Sørensen, A. Bodin, D. B. Trimarco, C. D. Damsgaard, P. C. K. Vesborg, O. Hansen, I. E. L. Stephens, J. Kibsgaard, I. Chorkendorff, *Nat. Catal.* **2018**, *1*, 820; b) X. Zhang, Y. Zhao, Y. Zhao, R. Shi, G. I. N. Waterhouse, T. Zhang, *Adv. Energy Mater.* **2019**, *9*, 1900881; c) W. Zhang, Y. Wu, J. Qi, M. Chen, R. Cao, *Adv. Energy Mater.* **2017**, *7*, 1602547; d) M. Görlin, P. Chernev, J. Ferreira de Araújo, T. Reier, S. Dresch, B. Paul, R. Krähnert, H. Dau, P. Strasser, *J. Am. Chem. Soc.* **2016**, *138*, 5603; e) F. Song, X. Hu, *Nat. Commun.* **2014**, *5*, 4477; f) K. Fominykh, J. M. Feckl, J. Sicklinger, M. Döbbling, S. Böcklein, J. Ziegler, L. Peter, J. Rathousky, E.-W. Scheidt, T. Bein, D. Fattakhova-Rohlfing, *Adv. Funct. Mater.* **2014**, *24*, 3123.
- [24] a) H. S. Ahn, A. J. Bard, *J. Am. Chem. Soc.* **2016**, *138*, 313; b) M. Asnavandi, Y. Yin, Y. Li, C. Sun, C. Zhao, *ACS Energy Lett.* **2018**, *3*, 1515; c) N. Li, D. K. Bediako, R. G. Hadt, D. Hayes, T. J. Kempa, F. von Cube, D. C. Bell, L. X. Chen, D. G. Nocera, *Proc. Natl. Acad. Sci. USA* **2017**, *114*, 1486.
- [25] a) F. Song, M. M. Busch, B. Lassalle-Kaiser, C.-S. Hsu, E. Petkucheva, M. Bensimon, H. M. Chen, C. Corminboeuf, X. Hu, *ACS Cent. Sci.* **2019**, *5*, 558; b) K. Fominykh, P. Chernev, I. Zaharieva, J. Sicklinger, G. Stefanic, M. Döbbling, A. Müller, A. Pokharel, S. Böcklein, C. Scheu, T. Bein, D. Fattakhova-Rohlfing, *ACS Nano* **2015**, *9*, 5180; c) S. Lee, K. Banjac, M. Lingenfelder, X. Hu, *Angew. Chem., Int. Ed.* **2019**, *58*, 10295; d) J. Y. C. Chen, L. Dang, H. Liang, W. Bi, J. B. Gerken, S. Jin, E. E. Alp, S. S. Stahl, *J. Am. Chem. Soc.* **2015**, *137*, 15090.
- [26] a) B. M. Hunter, J. R. Winkler, H. B. Gray, *Molecules* **2018**, *23*, 903; b) J. M. P. Martirez, E. A. Carter, *J. Am. Chem. Soc.* **2019**, *141*, 693; c) L. J. Enman, M. B. Stevens, M. H. Dahan, M. R. Nellist, M. C. Toroker, S. W. Boettcher, *Angew. Chem., Int. Ed.* **2018**, *57*, 12840.

- [27] Q. Shi, Q. Liu, Y. Ma, Z. Fang, Z. Liang, G. Shao, B. Tang, W. Yang, L. Qin, X. Fang, *Adv. Energy Mater.* **2020**, *10*, 1903854.
- [28] Y. Kwon, K. J. P. Schouten, J. C. van der Waal, E. de Jong, M. T. M. Koper, *ACS Catal.* **2016**, *6*, 6704.
- [29] a) A. J. E. Eerhart, A. P. C. Faaij, M. K. Patel, *Energy Environ. Sci.* **2012**, *5*, 6407; b) R.-J. van Putten, J. C. van der Waal, E. de Jong, C. B. Rasrendra, H. J. Heeres, J. G. de Vries, *Chem. Rev.* **2013**, *113*, 1499.
- [30] K. R. Vuyyuru, P. Strasser, *Catal. Today* **2012**, *195*, 144.
- [31] a) P. Zhang, X. Sheng, X. Chen, Z. Fang, J. Jiang, M. Wang, F. Li, L. Fan, Y. Ren, B. Zhang, B. J. J. Timmer, M. S. G. Ahlquist, L. Sun, *Angew. Chem., Int. Ed.* **2019**, *58*, 9155; b) N. Zhang, Y. Zou, L. Tao, W. Chen, L. Zhou, Z. Liu, B. Zhou, G. Huang, H. Lin, S. Wang, *Angew. Chem., Int. Ed.* **2019**, *58*, 15895; c) S. Barwe, J. Weidner, S. Cychy, D. M. Morales, S. Dieckhöfer, D. Hiltrop, J. Masa, M. Muhler, W. Schuhmann, *Angew. Chem., Int. Ed.* **2018**, *57*, 11460; d) W. Li, N. Jiang, B. Hu, X. Liu, F. Song, G. Han, T. J. Jordan, T. B. Hanson, T. L. Liu, Y. Sun, *Chem* **2018**, *4*, 637; e) W.-J. Liu, L. Dang, Z. Xu, H.-Q. Yu, S. Jin, G. W. Huber, *ACS Catal.* **2018**, *8*, 5533.
- [32] a) J. Bai, D. Liu, J. Yang, Y. Chen, *ChemSusChem* **2019**, *12*, 2117; b) Y. Wang, S. Zou, W.-B. Cai, *Catalysis* **2015**, *5*, 1507.
- [33] R. J. Cava, H. Takagi, H. W. Zandbergen, J. J. Krajewski, W. F. Peck, T. Siegrist, B. Batlogg, R. B. van Dover, R. J. Felder, K. Mizuhashi, J. O. Lee, H. Eisaki, S. Uchida, *Nature* **1994**, *367*, 252.
- [34] M. Armbrüster, R. Schlögl, Y. Grin, *Sci. Technol. Adv. Mater.* **2014**, *15*, 034803.
- [35] a) E. Edison, W. C. Ling, V. Aravindan, S. Madhavi, *ChemElectroChem* **2017**, *4*, 1932; b) S. Wang, M. He, M. Walter, F. Krumeich, K. V. Kravchik, M. V. Kovalenko, *Nanoscale* **2018**, *10*, 6827.
- [36] F. Song, K. Schenk, X. Hu, *Energy Environ. Sci.* **2016**, *9*, 473.
- [37] P. W. Menezes, C. Panda, S. Garai, C. Walter, A. Guet, M. Driess, *Angew. Chem., Int. Ed.* **2018**, *57*, 15237.
- [38] K. Karthick, S. Anantharaj, S. Patchaiammal, S. N. Jagadeesan, P. Kumar, S. R. Ede, D. K. Pattanayak, S. Kundu, *Inorg. Chem.* **2019**, *58*, 9490.
- [39] F. T. Seitz, D. Turnbull, H. Ehrenreich, *Solid State Physics*, Academic Press, New York **1968**.
- [40] N. H. Chou, R. E. Schaak, *J. Am. Chem. Soc.* **2007**, *129*, 7339.
- [41] M. Armbrüster, W. Schnelle, R. Cardoso-Gil, Y. Grin, *Chem. - Eur. J.* **2010**, *16*, 10357.
- [42] M. Armbrüster, M. Schmidt, R. Cardoso-Gil, H. Borrmann, Y. Grin, *Z. Kristallogr. - New Cryst. Struct.* **2007**, *222*, 83.
- [43] Y. Yin, R. M. Rioux, C. K. Erdonmez, S. Hughes, G. A. Somorjai, A. P. Alivisatos, *Science* **2004**, *304*, 711.
- [44] a) A. T. Brown, K. G. Barron, B. G. Salazar, P. Kirby, G. T. McCandless, A. V. Walker, J. Y. Chan, *Z. Anorg. Allg. Chem.* **2017**, *643*, 2038; b) C. Wang, J. Wang, H. Chen, M. Wen, K. Xing, S. Chen, Q. Wu, *Sci. China Mater.* **2016**, *59*, 927; c) C. Leostean, O. Pana, M. Stefan, A. Popa, D. Toloman, M. Senila, S. Gutoiu, S. Macavei, *Appl. Surf. Sci.* **2018**, *427*, 192.
- [45] K. K. D. Ehinon, S. Naille, R. Dedryvère, P.-E. Lippens, J.-C. Jumas, D. Gonbeau, *Chem. Mater.* **2008**, *20*, 5388.
- [46] P. Li, X. Duan, Y. Kuang, Y. Li, G. Zhang, W. Liu, X. Sun, *Adv. Energy Mater.* **2018**, *8*, 1703341.
- [47] J. Kibsgaard, I. Chorkendorff, *Nat. Energy* **2019**, *4*, 430.
- [48] a) J. Masud, S. Umapathi, N. Ashokaan, M. Nath, *J. Mater. Chem. A* **2016**, *4*, 9750; b) D. Zhong, L. Liu, D. Li, C. Wei, Q. Wang, G. Hao, Q. Zhao, J. Li, *J. Mater. Chem. A* **2017**, *5*, 18627; c) C. Zhang, B. Zhang, Z. Li, J. Hao, *ACS Appl. Energy Mater.* **2019**, *2*, 3343; d) J. Zou, G. Peleckis, C.-Y. Lee, G. G. Wallace, *Chem. Commun.* **2019**, *55*, 8808; e) M. Abu Sayeed, G. J. Millar, A. P. O'Mullane, *ChemElectroChem* **2019**, *6*, 3667.
- [49] C. Feng, M. B. Faheem, J. Fu, Y. Q. Xiao, C. L. Li, Y. B. Li, *ACS Catal.* **2020**, *10*, 4019.
- [50] a) Q. Kang, L. Vernisse, R. C. Remsing, A. C. Thenuwara, S. L. Shumlas, I. G. McKendry, M. L. Klein, E. Borguet, M. J. Zdilla, D. R. Strongin, *J. Am. Chem. Soc.* **2017**, *139*, 1863; b) Y. Yoon, B. Yan, Y. Surendranath, *J. Am. Chem. Soc.* **2018**, *140*, 2397.
- [51] a) P. W. Menezes, C. Walter, J. N. Hausmann, R. Beltran-Suito, C. Schlesiger, S. Praetz, V. Y. Verchenko, A. Shevelkov, M. Driess, *Angew. Chem., Int. Ed.* **2019**, *58*, 16569; b) C. Panda, P. W. Menezes, M. Zheng, S. Orthmann, M. Driess, *ACS Energy Lett.* **2019**, *4*, 747; c) X. Xu, F. Song, X. Hu, *Nat. Commun.* **2016**, *7*, 12324.
- [52] a) D. L. A. de Faria, F. N. Lopes, *Vib. Spectrosc.* **2007**, *45*, 117; b) D. L. A. de Faria, S. Venâncio Silva, M. T. de Oliveira, *J. Raman Spectrosc.* **1997**, *28*, 873; c) W. Luo, C. Jiang, Y. Li, S. A. Shevlin, X. Han, K. Qiu, Y. Cheng, Z. Guo, W. Huang, J. Tang, *J. Mater. Chem. A* **2017**, *5*, 2021.
- [53] a) M. B. Stevens, L. J. Enman, A. S. Batchellor, M. R. Cosby, A. E. Vise, C. D. M. Trang, S. W. Boettcher, *Chem. Mater.* **2017**, *29*, 120; b) P. Yu, Z. Zhang, L. Zheng, F. Teng, L. Hu, X. Fang, *Adv. Energy Mater.* **2016**, *6*, 1601111.
- [54] S. Klaus, L. Trotochaud, M.-J. Cheng, M. Head-Gordon, A. T. Bell, *ChemElectroChem* **2016**, *3*, 66.
- [55] R. D. L. Smith, M. S. Prévot, R. D. Fagan, Z. Zhang, P. A. Sedach, M. K. J. Siu, S. Trudel, C. P. Berlinguette, *Science* **2013**, *340*, 60.
- [56] W. Ye, Y. Yang, X. Fang, M. Arif, X. Chen, D. Yan, *ACS Sustainable Chem. Eng.* **2019**, *7*, 18085.
- [57] R. Gao, H. Zhang, D. Yan, *Nano Energy* **2017**, *31*, 90.
- [58] C. C. L. McCrory, S. Jung, J. C. Peters, T. F. Jaramillo, *J. Am. Chem. Soc.* **2013**, *135*, 16977.
- [59] a) P. W. Menezes, A. Indra, C. Das, C. Walter, C. Göbel, V. Gutkin, D. Schmeißer, M. Driess, *ACS Catal.* **2017**, *7*, 103; b) P. W. Menezes, C. Panda, C. Walter, M. Schwarze, M. Driess, *Adv. Funct. Mater.* **2019**, *29*, 1808632.
- [60] a) T. Wu, S. Sun, J. Song, S. Xi, Y. Du, B. Chen, W. A. Sasangka, H. Liao, C. L. Gan, G. G. Scherer, L. Zeng, H. Wang, H. Li, A. Grimaud, Z. J. Xu, *Nat. Catal.* **2019**, *2*, 763; b) Z. Wu, Q. Gan, X. Li, Y. Zhong, H. Wang, *J. Phys. Chem. C* **2018**, *122*, 2848; c) Z. Wu, X. Li, W. Liu, Y. Zhong, Q. Gan, X. Li, H. Wang, *ACS Catal.* **2017**, *7*, 4026; d) B. Yan, D. Krishnamurthy, C. H. Hendon, S. Deshpande, Y. Surendranath, V. Viswanathan, *Joule* **2017**, *1*, 600.
- [61] D. Fu, P. G. Keech, X. Sun, J. C. Wren, *Phys. Chem. Chem. Phys.* **2011**, *13*, 18523.
- [62] Q. Xiang, F. Li, W. Chen, Y. Ma, Y. Wu, X. Gu, Y. Qin, P. Tao, C. Song, W. Shang, H. Zhu, T. Deng, J. Wu, *ACS Energy Lett.* **2018**, *3*, 2357.